

# The sensitivity of sprite streamer inception on the initial electronion patch

**Köhn, C.; Chanrion, Olivier; Neubert, T.**

*Published in:*
Journal of Geophysical Research: Space Physics

*Link to article, DOI:*
10.1029/2018JA025972

*Publication date:*
2019

*Document Version*
Publisher's PDF, also known as Version of record

JGR Space Physics

RESEARCH ARTICLE
10.1029/2018JA025972

# The Sensitivity of Sprite Streamer Inception on the Initial Electron-Ion Patch

C. Köhn[1], O. Chanrion[1], and T. Neubert[1]

[1]National Space Institute (DTU Space), Technical University of Denmark, Kongens Lyngby, Denmark

**Key Points:**
- The speed of the streamer motion depends on the geometry of the initial electron-ion patch
- The development of the electric field in the early streamer stages is fastest for prolate patches
- Ohmic heating is most significant for streamers from prolate patches and least significant for streamers from oblate patches

**Supporting Information:**
- Supporting Information S1
- Movie S1

**Correspondence to:**
C. Köhn,
koehn@space.dtu.dk

**Citation:**
Köhn, C., Chanrion, O., & Neubert, T. (2019). The sensitivity of sprite streamer inception on the initial electron-ion patch. *Journal of Geophysical Research: Space Physics*, *124*, 3083–3099. https://doi.org/10.1029/2018JA025972

Received 3 AUG 2018
Accepted 19 MAR 2019
Accepted article online 6 APR 2019
Published online 29 APR 2019



**Abstract** Sprite streamers are bright atmospheric phenomena above thunderstorms powered by sufficiently high electric fields and free charges from inhomogeneities in the mesosphere or ionosphere. A common feature of recent simulations is that they model the streamer inception from spherical Gaussian electron-ion patches. We here tackle the following question: How do the streamer inception time and streamer properties depend on the initial geometry? Therefore, we consider prolate ("cigar") and oblate ("pancake") electron-ion patches aiming to understand the geometric influence on streamer inception speed, electric field evolution, branching time, and ohmic heating of streamers. We initiate patches of different geometry with fixed peak densities of $5 \cdot 10^{11}$ m$^{-3}$ or with a fixed total electron number of $9.40 \cdot 10^{12}$ in ambient fields of 0.5 and 1.5 times the breakdown field and study the streamer evolution between 60 and 80 km altitude with a 2.5D cylindrical Monte Carlo particle code. We present the evolution of the electron density and of the electric field. In our simulations, the time for the electric field tips to develop into the regime where they can self sustain the discharge is shortest for streamers from prolate patches and longest for oblate patches. The branching time of negative fronts depends on the eccentricity and increases for oblate patches ranging from 5 to 8 $\mu$s. We observe ohmic heating with maximum temperature differences up to tens of kelvins depending on the eccentricity and density of the initial patch influencing the efficiency of plasma reactions in streamer channels.

## 1. Introduction

Transient luminous events are luminous atmospheric phenomena extending several kilometers above thunderclouds and become manifest in sprites, blue jets, or gigantic jets (Celestin & Pasko, 2011; Cummer et al., 2006; Ebert & Sentman, 2008; Luque & Ebert, 2009; Lyons, 1996; Neubert, 2003; Pasko, 2007, 2008; Qin et al., 2012; Sentman et al., 1995;). Among these, sprite discharges form in the mesosphere and ionosphere, between approximately 60 and 90 km (see, e.g., Cummer et al., 2006; Stenbaek-Nielsen et al., 2013). They consist of streamer discharges, channels with a quasi-neutral interior and with high electric fields at their tips. These discharges were first predicted by Wilson (1925). Electrostatic fields are generated by the removal of charge through positive cloud-to-ground lightning (+CG) and decrease with altitude as $h^{-3}$ while the breakdown field changes as $\exp(-h/H)$ where $H$ is the scale height; thus, there is an intersection altitude where the ambient field generated by charge removal exceeds the breakdown field making it possible for sprite streamers to develop and grow. Sprites were first reported by Vaughan and Vonnegut (1989) as well as by Franz et al. (1990) and confirmed later by various other missions (Blanc et al., 2007; Boeck et al., 1998; Stenbaek-Nielsen et al., 2013; Yair et al., 2003).

First simulations were performed by Pasko et al. (1995, 1997). Using a quasi-electrostatic model, they found that fields induced by +CG lightning significantly energize electrons and produce secondary electrons by ionization laying the basics for the inception and evolution of sprite discharges. Further simulations were subsequently performed by Liu and Pasko (2004); Luque and Ebert (2010); Liu et al. (2012); Kosar et al. (2013); Liu et al. (2015).

A common feature of most simulations is that the charge density of the initial electron-ion patch is a spherical Gaussian although it is known that already a few electrons, or even one single electron, are sufficient to start an electron avalanche and subsequently a streamer discharge (e.g., Li et al., 2008). The probability of streamer inception from a few electrons is due to the interplay between ionization and attachment: While an electron is accelerated in the ambient electric field, it first reaches the attachment threshold energy before it reaches the energy regime of ionization. If it by chance overcomes the critical energy for attachment, it

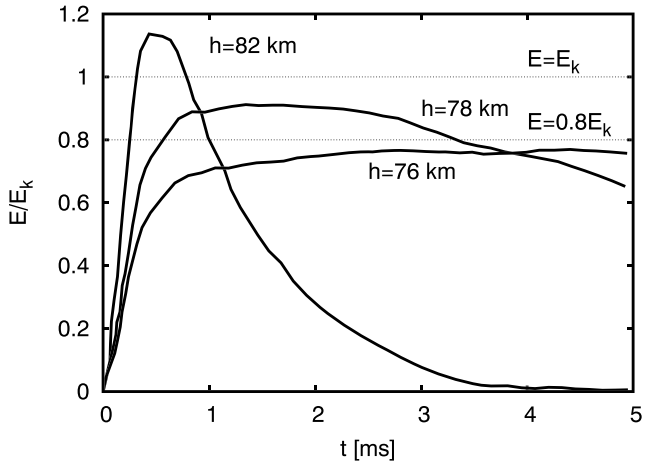


**Figure 1.** The temporal evolution of the electric field induced by a +CG flash at different altitudes. The charge moment change of this particular +CG flash is 458.7 C km within the first 5 ms. The values were calculated in (Qin et al., 2013b). The dotted lines show $0.8E_k$ and $1E_k$.

can ionize an air molecule and produce an additional electron. In turn, the primary and secondary electron may again overcome the critical energy for attachment and ionize air. After 18–20 avalanche lengths, known as the the Raether-Meek criterion (Meek, 1940; Raether, 1939), space charge effects set in, and the electron avalanche turns into a streamer. Hence, the creation of an electron avalanche and of a streamer developing from an electron avalanche is a random process not necessarily fulfilled by one free electron. Thus, it is computationally cheaper to start simulations with a spherical Gaussian seed.

In nature, initial seed electrons for sprite streamers can be provided by local inhomogeneities whose origin is not fully understood yet and is a fundamental problem in itself: These can be trails of meteors (Suszcynsky et al., 1999) or remnants of previous sprite streamers (Stenbaek-Nielsen et al., 2000). High-speed camera observations by McHarg et al. (2002), by Cummer et al. (2006), and by Qin et al. (2014) have shown inhomogeneities, which are extended vertically instead of being spherical; therefore, we here focus on studying the effects of the initial geometry of such inhomogeneities.

Besides their initial spatial distribution, electrons need to encounter an electric field sufficiently large and for a period long enough to energize them into the energy regime where they can create sufficient ionization and further develop into a streamer with its own self-sustained electric field. At this stage, the electric field at the tips helps to sustain the streamer propagation; however, the development into the streamer mode needs sufficient time. Qin et al. (2013a) have shown that for negative streamers at 75 km altitude the electric field needs to be at least 0.8 times the breakdown field. Figure 1 shows a sketch of an electric field (Qin et al., 2013b) induced by a +CG flash at different altitudes. Although the timescale of electric fields is in the order of milliseconds, the time scale of the fields to be above 0.8 times the breakdown field or even above the breakdown is in the order of milliseconds down to microseconds if at all.

Since sprite streamers form from electron avalanches with space charge effects contributing significantly after 18–20 avalanche lengths, electrons need to encounter the ambient field for a certain period of time. Considering that the initial electrons come from nonspherical inhomogeneities, we here post the following question: How realistic is the assumption of a spherical Gaussian patch, and how does the growth of the electron density relate to the available time of the ambient field? We here take one step to a more realistic scenario and use ellipsoidal patches with different eccentricity and study the evolution of the electric field and the inception of streamers in mesospheric electric fields and relate this to the streamer inception time. This approach is similar to the one by Kosar et al. (2012); however, in their work, they simulate streamers from prolate electron-ion patches in subbreakdown fields only with focus on the streamer speed and brightness during the whole streamer evolution.

Furthermore, after their inception, sprite streamers propagate through air and form visible structures of different shapes, such as carrot sprites, jellyfish sprites, angle sprites, or column sprites (Bor, 2013; McHarg et al., 2002; Pasko et al., 2000; Qin et al., 2013b; Stenbaek-Nielsen et al., 2000; Su et al., 2002). An extensive overview of the physics of different morphologies is given in a review paper by Pasko et al. (2013). But to what extent does the morphology depend on the shape of the initial charged patch?

Apart from the streamer inception and streamer morphology, various authors have studied the air heating and the plasma chemistry associated to sprite streamers. Air heating is a process divided into two different timescales: a fast heating process where energy is transferred from charged to neutral species and a delayed process where energy is transferred through the relaxation from vibrational to translational states (da Silva & Pasko, 2013). It generates infrasonic acoustic waves, which can be used to detect sprites (da Silva & Pasko, 2014) and enables plasma chemistry such as the production and emission of $NO_x$ and its effects on the climate (Armstrong, 2000; Armstrong et al., 2001; Gordiollo-Vázquez, 2008; Rodger et al., 2008; Sentman et al., 2008; Winkler & Notholt, 2014). Since the efficiency of chemical reactions depends on the heating of streamers, we determine the maximum temperature increase through ohmic heating depending on the initial conditions and its influence on the reaction rates.

**Table 1**
*The Electron Mobility $\mu$, the Electron Diffusion D, and the Effective Townsend Coefficient $\alpha_{eff} = \alpha_{ion} - \alpha_{att}$, With the Ionization Coefficient $\alpha_{ion}$ and the Attachment Coefficient $\alpha_{att}$ (Luque & Ebert, 2009) at Ground Level, at 60 km Altitude, and at 80 km Altitude*

| Parameter | Value at ground | Value at 60 km altitude | at 80 km |
|---|---|---|---|
| Electron mobility $\mu$ ($m^2 \cdot V^{-1} \cdot s^{-1}$) | 0.038 | 51.05 | 563.27 |
| Electron diffusion $D$ ($m^2\ s^{-1}$) | 0.18 | 241.79 | 2,667.85 |
| Effective Townsend coefficient $\alpha_{eff}$ ($m^{-1}$) | 431,200 | 0.03 | 0.003 |

Since sprite streamers initiate between 60 and 80 km altitude, the current work is focused on the inception time and on the properties of sprite streamers at 60 km altitude as a lower limit and at 80 km altitude as an upper limit. However, through scaling laws, our argumentation is general and thus applicable to streamer discharges at different altitudes (see, e.g., Liu & Pasko, 2004).

In section 2 we describe our model. We recall the Raether-Meek criterion and define the computational domain and how we implement different initial ellipsoidal electron-ion patches. In section 3 we present the streamer inception time as well as the temporal evolution of the electric field, the branching time, and ohmic heating. Finally, we discuss and conclude these results in section 4.

## 2. Modeling

### 2.1. The Raether-Meek Criterion: From Electron Avalanches to Streamers

Starting from a single electron, an electron avalanche develops in an ambient field $E_{amb}$ through electron impact ionization of air molecules. Including ionization and diffusion, but excluding space charge effects, the density $n_e^1$ of the electron avalanche in cylindrical coordinates $(r, z)$ becomes (Raizer, 1991)

$$n_e^1(r,z,t) = \left(\frac{1}{\sqrt{4\pi D t}}\right)^3 e^{-\frac{r^2+(z-\mu E_{amb} t)^2}{4Dt}} e^{\alpha_{eff}\mu E_{amb} t} \tag{1}$$

after time $t$. Here we use the same diffusion coefficient $D$, electron mobility $\mu$, and effective Townsend coefficient $\alpha_{eff}$ as in Luque and Ebert (2009), summarized in Table 1.

Once sufficient charge is created; the electron avalanche enters the streamer regime where space charge effects start to play a significant role. Starting from one single electron, the usual assumption is that approximately 18–20 avalanches are needed before an electron avalanche transits into a streamer. Hence, the moment of time of this transition is given through

$$t \lesssim \frac{18-20}{\alpha_{eff}\mu E_{amb}}, \tag{2}$$

which is known as the Raether-Meek criterion (Meek, 1940; Raether, 1939). The characteristic size $\lambda$ of the electron avalanche, before the space charge effects set in, is then determined by diffusion and equals to

$$\lambda = \sqrt{4Dt} \lesssim \sqrt{4D \cdot \frac{18-20}{\alpha_{eff}\mu E_{amb}}}. \tag{3}$$

### 2.2. The Geometry of the Initial Charge Patches

In order to study the inception time and properties of sprite streamers at 60 and 80 km altitude, we have performed numerous simulations initiated from Gaussian electron-ion patches

$$n_i^0(r,z,t=0) = n_e^0(r,z,t=0) = n_{e,0} e^{-\frac{r^2}{\lambda_r^2} - \frac{(z-z_0)^2}{\lambda_z^2}} \tag{4}$$

with $z_0 = L_z/2$ and varying $n_{e,0}$, $\lambda_r$, and $\lambda_z$. Figure 2 sketches the initial electron density at 60 km altitude: We use a cylindrical simulation domain, which is $L_r = 100$ m in $r$ and $L_z = 200$ m in $z$ direction at 60 km altitude and $L_r$= 1,000 m as well as $L_z$ = 2,000 m at 80 km altitude, and vary $\lambda_r$ and $\lambda_z$ to discuss streamers for (a) spherical, (b) prolate ("cigar"), and (c) oblate ("pancake") electron-ion patches. At 60 km altitude and in a field of 1.5 times the breakdown field, the maximum size (3) of the electron avalanche before space charges become important is $\lambda \approx 1.8$ m. As a reference simulation, we therefore use a spherical Gaussian

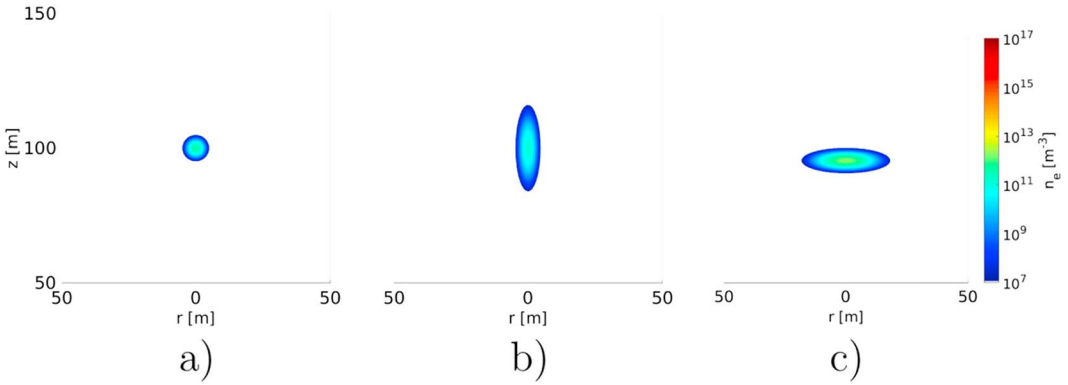


**Figure 2.** Part of the simulation domain and the initial electron density (4) for a (a) spherical, (b) prolate (cigar), and (c) oblate (pancake) electron-ion patch.

with $\lambda_r = \lambda_z = 1.5$ m; as initial density, we choose $n_{e,0} = 5 \cdot 10^{11}$ m$^{-3}$ as in Liu and Pasko (2004); for this particular geometry, the initial electron number is thus $N_{e,0} \approx 9.40 \cdot 10^{12}$. However, fixing $n_{e,0}$ and varying $\lambda_r$ or $\lambda_z$ changes the total initial electron number, which successively changes streamer properties, such as the propagation velocity (Luque et al., 2008; Qin et al., 2013a). This might falsify our interpretation of pure geometric effects; hence, we have additionally performed simulations with the fixed electron number $N_{e,0}$ rather than with the peak electron density $n_{e,0}$. At 80 km altitude, (3) becomes ≈ 19 m; that is why we choose $\lambda_r = \lambda_z = 15$ m as a reference simulation with $n_{e,0} = 5 \cdot 10^{10}$ m$^{-3}$ and $N_{e,0} \approx 9.40 \cdot 10^{14}$.

### 2.3. Setup of the Model

We simulate the motion of electrons in air at 60 and 80 km altitude. After every time step, we solve the Poisson equation for the electrostatic potential $\phi$ on a mesh with 200 grid points in $r$ and 1,200 grid points in $z$ direction. At the boundaries ($z = 0, L_z$) we use the Dirichlet boundary conditions $\phi(r, 0) = 0$ and $\phi(r, L_z) = E_{amb} \cdot L_z$ where $E_{amb}$ is the ambient electric field pointing downward, and at ($r = 0, L_r$) we use the Neumann boundary conditions $\partial\phi/\partial r = 0$. We have performed simulations in ambient fields of $0.5E_k$ and $1.5E_k$ where $E_k \approx 2{,}382.20$ V m$^{-1}$ and $E_k \approx 215.90$ V m$^{-1}$ are the breakdown fields at 60 and 80 km altitude, respectively, implying a scale height of 8.33 km.

We trace individual (super)electrons (Chanrion & Neubert, 2008) through air with a 2.5D particle-in-cell Monte Carlo code with cylindrical symmetry with two spatial coordinates $(r, z)$ and with three velocity coordinates $(v_r, v_\theta, v_z)$. We have included excitations of air molecules, elastic collisions of electrons, electron impact ionization, electron attachment, and bremsstrahlung. Additionally, we have implemented the photoionization of air molecules through bremsstrahlung photons and through UV photons emitted by excited nitrogen. More details about the implementation can be found in Chanrion and Neubert (2008) and Köhn et al. (2017). Due to limited computer resources, we merge individual electrons close in phase space to super electrons. Contrarily, in order to reduce computational noise, we split super electrons, which solely populate one single grid cell. Details about the implementation of the merging and splitting scheme can be found in Chanrion and Neubert (2008) and Köhn et al. (2017).

The time for the detachment of electrons from oxygen ions can be estimated through (Sun et al., 2014)

$$t_D = \frac{1}{k_6 \cdot 0.2 \cdot n_B + k_7 \cdot 0.8 \cdot n_B} \tag{5}$$

with (Kossyi et al., 1992)

$$k_6 = 2.7 \cdot 10^{-10} \sqrt{T/300\,\mathrm{K}} \exp\left(-5590\mathrm{K}/T\right) \mathrm{cm}^3\mathrm{s}^{-1}, \tag{6}$$

$$k_7 = 1.9 \cdot 10^{-12} \sqrt{T/300\,\mathrm{K}} \exp\left(-4990\mathrm{K}/T\right) \mathrm{cm}^3\mathrm{s}^{-1} \tag{7}$$

and

$$T = T_{amb} + \frac{1}{3k_B} M_{ion} \left(\mu_{ion} E\right)^2, \tag{8}$$

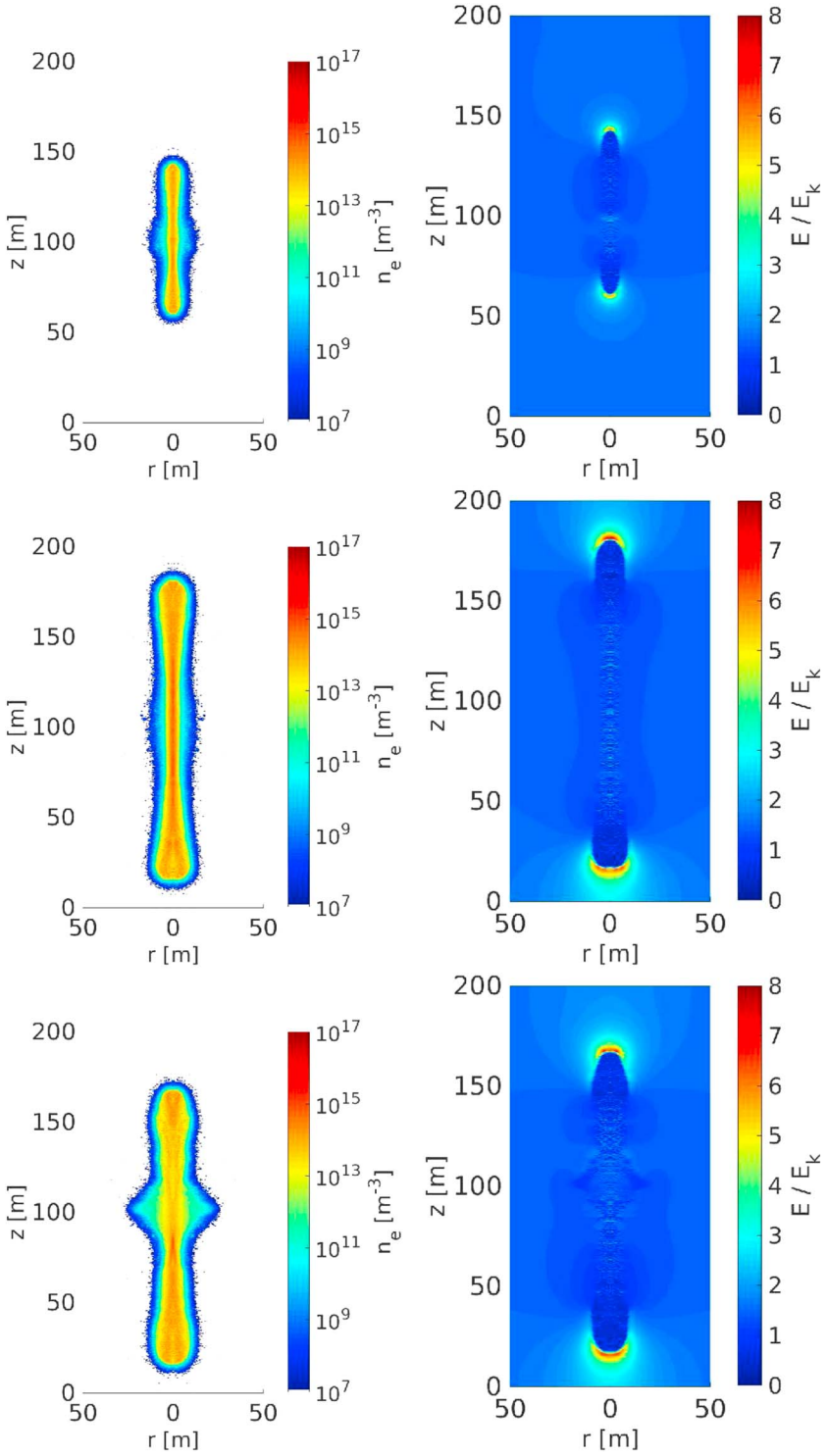


**Figure 3.** The electron density (left column) and the electric field (right column) at 60 km altitude after 8.36 $\mu$s for a spherical ($\lambda_r = \lambda_z = 1.5$ m; first row), for a prolate ($\lambda_r = 1.5$ m, $\lambda_z = 5.25$ m; second row), and for an oblate ($\lambda_r = 5.25$ m, $\lambda_z = 1.5$ m; third row) initial electron-ion patch. Its peak density is $n_{e,0} = 5 \cdot 10^{11}$ $m^{-3}$, and the ambient field is $1.5E_k$ pointing downward.

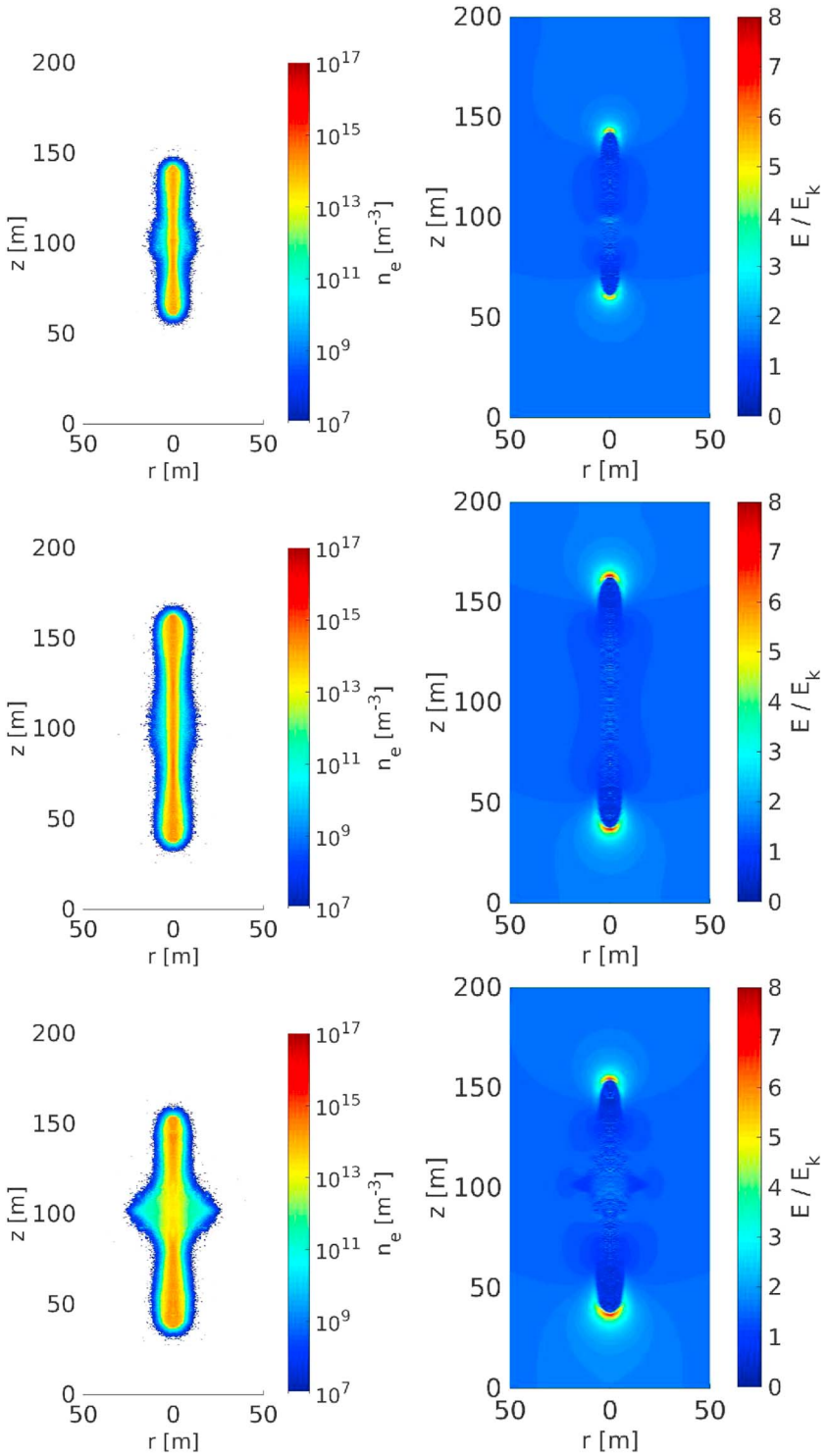


**Figure 4.** The electron density (left column) and the electric field (right column) after 8.36 $\mu$s for the same geometries and electric field as in Figure 3, now with a fixed initial electron number of $N_{e,0} = 9.40 \cdot 10^{12}$.

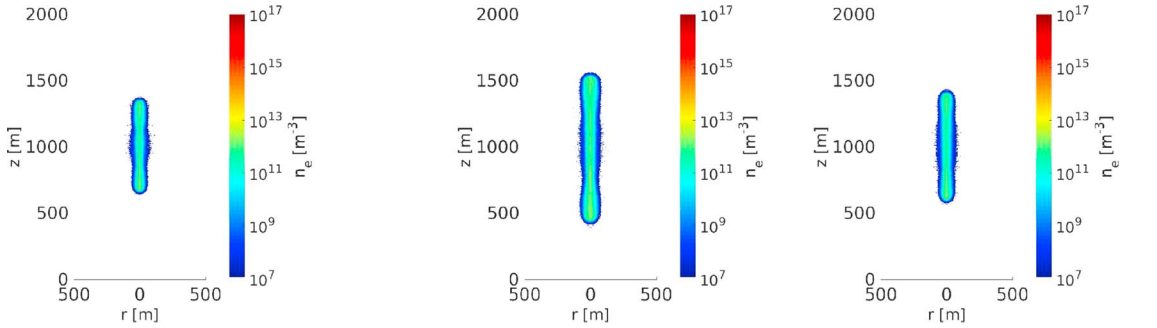


a) $\lambda_r = \lambda_z = 15$ m ($n_{e,0} = 5 \cdot 10^{10}$ m$^{-3}$, $N_{e,0} = 9.40 \cdot 10^{14}$)

b) $\lambda_r = 15$ m, $\lambda_z = 52.5$ m $n_{e,0} = 5 \cdot 10^{10}$ m$^{-3}$

c) $\lambda_r = 15$ m, $\lambda_z = 52.5$ m $N_{e,0} = 9.40 \cdot 10^{14}$

**Figure 5.** The electron density at 80 km altitude after 65.40 $\mu$s for a (a) spherical ($\lambda_r = \lambda_z = 15$ m) and for a (b and c) prolate ($\lambda_r = 15$ m, $\lambda_z = 52.5$ m) initial electron-ion patch with peak densities $n_{e,0}$ and electron number $N_{e,0}$. The ambient field amounts to $1.5E_k$.

where $\mu_{ion} \approx 0.1$ m$^2$ (Vs)$^{-1}$ is the ion mobility at approximately 60 km altitude, $k_B \approx 1.38 \cdot 10^{-23}$ J K$^{-1}$ is the Boltzmann constant, $M_{ion} \approx 16 \cdot 1.67 \cdot 10^{-27}$ kg is the ion mass, $T_{amb} = 247.02$ is the ambient temperature at 60 km altitude (www.engineeringtoolbox.com/standard-atmosphere-d_604.html), and $E$ is the electric field. The detachment time $t_D$ amounts to approximately 2,447 s for $E = 0.5E_k$, 19 s for $E = 1.5E_k$, 11 ms for $E = 3E_k$, and 15 $\mu$s for $E = 6E_k$, which is in all cases longer than the simulated time. Since the density and the temperature decrease from 60 to 80 km altitude, detachment is also negligible at 80 km altitude. Thus, detachment does not play a significant role in the interpretation of our simulation results.

## 3. Results

### 3.1. Streamer Development for Different Geometries and Different Initial Amount of Charges

Figure 3 shows the electron density and the electric field at 60 km altitude after 8.36 $\mu$s for different initial geometries in an ambient field of $1.5E_k$ for a peak density of $n_{e,0} = 5 \cdot 10^{11}$ m$^{-3}$. This corresponds to a total initial electron number of $9.40 \cdot 10^{12}$ for the spherical electron-ion patch and to $3.29 \cdot 10^{13}$ as well as to $1.15 \cdot 10^{14}$ for the prolate and for the oblate patch, respectively. In our simulations, the initial electron-ion patch evolves into a double-headed streamer with negative polarity on the upper side and positive polarity on the lower side. The comparison shows that the streamer fronts move furthest for $\lambda_r \neq \lambda_z$. This is not surprising since for fixed $n_{e,0}$ the cigar and pancake patches contain more initial electrons than the spherical one and thus drive the streamer more efficiently through charge separation (Luque et al., 2008; Qin et al., 2013a). Additionally, Figure 3 shows that increasing the initial charge yields larger radii and larger electric fields at the positive and negative tips as compared to the streamer originating from a spherical patch.

We are left with the question whether the increased fields and velocities are an artifact of the increased initial electron number. To invalidate this possibility, we have run simulations with the same geometries as in Figure 3, but now fixing the initial electron number to $N_{e,0} = 9.40 \cdot 10^{12}$. As a supporting information, we have attached a movie file comparing the temporal evolution of the electron density for $\lambda_r = \lambda_z = 1.5$ m and for $\lambda_r = 5.25$ m, $\lambda_z = 1.5$ m for fixed $N_{e,0}$.

For such simulations, Figure 4 shows the electron density as well as the electric field after 8.36 $\mu$s. We observe the same tendency as in Figure 3: The streamers have extended further, and the electric field at the tips is more enhanced for streamers from nonspherical Gaussians. However, the spatial extension both in $r$ and $z$ is not as significant as for fixing the peak density $n_{e,0}$.

Figure 5 shows the electron density at 80 km altitude from a spherical electron-ion patch (a) and from a prolate electron-ion patch (b and c) for a fixed electron density (a and b) and for a fixed electron number (a and c). It illustrates the same tendency that we have observed for streamers at 60 km altitude. Panels (b) and (c) show that streamers from prolate patches develop faster than from spherical patches where fixing the initial electron density, that is, increasing the initial charge, additionally accelerates the streamer motion. Additionally, the comparison of Figures 3 and 4 with Figure 5 illustrates the scaling laws of streamers at different altitudes. Whereas the streamers at 60 km altitude move some tens of meter within some

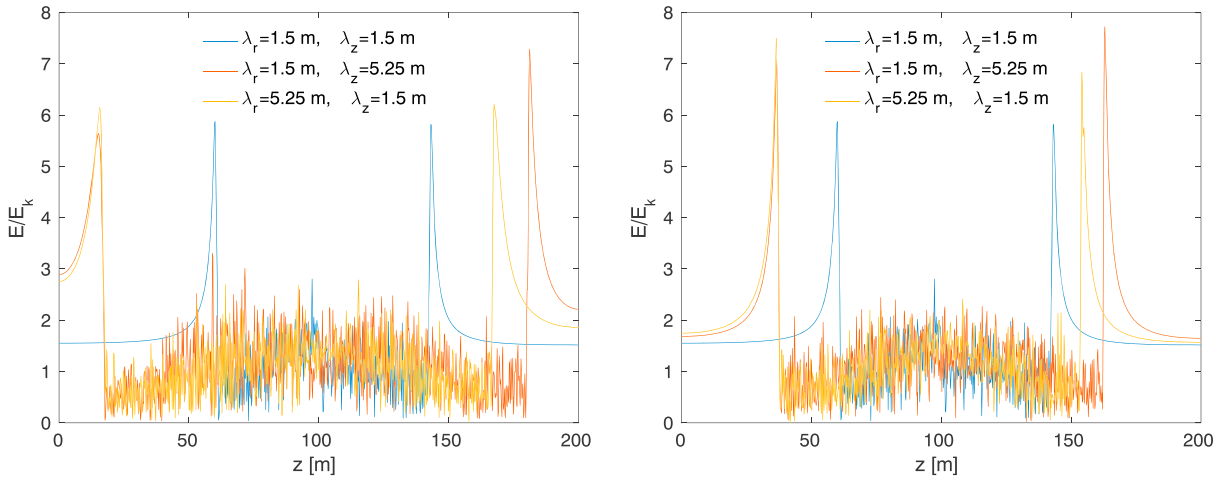


**Figure 6.** The on-axis electric field after 8.36 $\mu$s for the same conditions as in Figures 3a and 4b. In both panels, the left peaks display the positive front, and the right peaks the negative front. Note that for $\lambda_r = \lambda_z = 1.5$ m, the initial density $n_{e,0} = 5 \cdot 10^{11}$ m$^{-3}$ corresponds to the total electron number of $N_{e,0} = 9.40 \cdot 10^{12}$.

microseconds, streamers at 80 km altitude move hundreds of meter within tens of microseconds. This factor 10 is approximately the same factor as the ratio between the air density at 60 km altitude and at 80 km altitude.

For better visibility, Figure 6 displays the on-axis electric field after 8.36 $\mu$s. Panel (a) shows the fronts for fixed $n_{e,0}$, and panel (b) for fixed $N_{e,0}$. For both cases, the fields are higher in case of nonspherical initial patches. However, this effect is more pronounced for the negative front. After 8.36 $\mu$s both the positive and negative streamer fronts from the spherical patch moved approximately 40 m and reached an electric field of $5.85E_k$. In comparison, for fixed $n_{e,0}$, the negative fronts from the oblate and prolate patches moved 67 and 81 m and reached field values of $6.2E_k$ and $7.3E_k$ whereas the positive fronts for both geometries moved approximately 85 m and reached field values between $5.6E_k$ and $6.2E_k$. In all these cases, the amount of initial charge is higher for the nonspherical electron-ion patches; thus, the development is faster, which agrees with earlier simulation results by Luque et al. (2008). Panel (b), however, shows that we see a similar effect, even though not as apparent, for fixing the initial charge: Here the negative fronts from oblate and prolate patches moved 54 and 63 m and reached field values of $6.8E_k$ and $7.7E_k$ whereas the positive fronts moved 65 m and reached field values between $7.1E_k$ and $7.5E_k$.

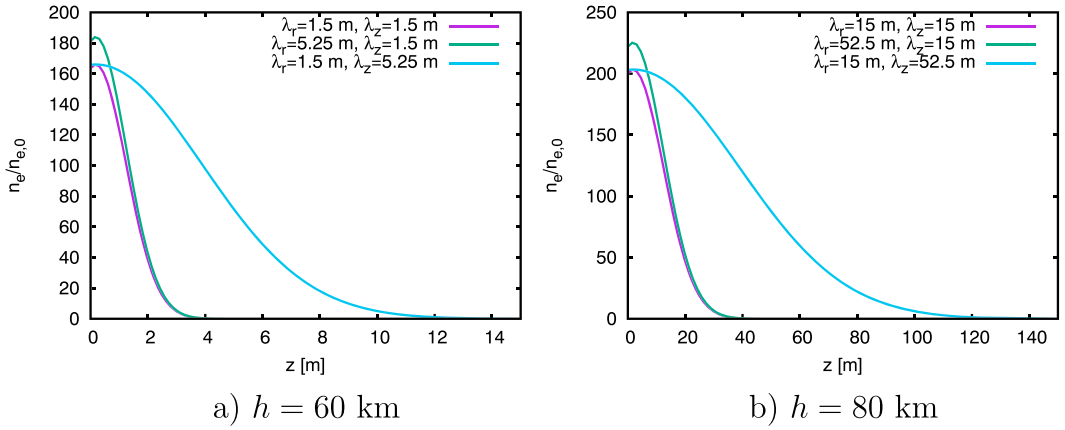


**Figure 7.** (a) The analytic solution (11) of the electron density at 60 km altitude normalized with the initial electron density $n_{e,0}$ after 1 $\mu$s as a function of $z$ for $r = 0.5$ m, $E_{amb} = 1.5E_k$, and three different geometries. (b) The same plot at 80 km altitude after 10 $\mu$s for $r = 5$ m.

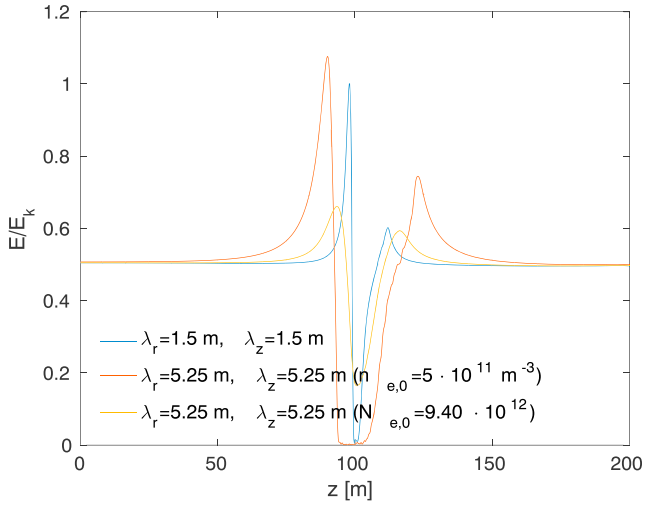


**Figure 8.** The on-axis electric field after 93.13 $\mu$s in an ambient field of $0.5E_k$ at 60 km altitude for different patch geometries and initial charges. The left peaks show the positive fronts, and the right peaks the negative front.

In first approximation, we can compare these results for early time steps with an analytic solution for the electron density neglecting space charge effects. Since equation (1) only gives the electron density originating from one single electron, we convolve the electron density (1) with the initial electron density (4) used in our simulations and obtain the electron density for early time steps:

$$n_e(r,z,t) = \int_{\mathbb{R}^3} d^3\mathbf{r}' \quad n_e^1(r-r',z-z',t)\cdot n_e^0(r',z',t=0) \tag{9}$$

$$= 2\pi \int_{r'=0}^{\infty}\int_{z'=-\infty}^{\infty} n_e^1(r-r',z-z',t)\cdot n_e^0(r',z',t=0)r'dr'dz' \tag{10}$$

$$\begin{aligned} = & \frac{2\pi}{2D^2t^2(4Dt+\lambda_r^2))\sqrt{\frac{1}{Dt}+\frac{4}{\lambda_r^2}}\sqrt{\frac{1}{Dt}+\frac{4}{\lambda_z^2}}}\left[n_{e,0}\sqrt{Dt}\lambda_r^2\sqrt{\pi}r\right. \\ \times & \left(2Dt\sqrt{\frac{1}{Dt}+\frac{4}{\lambda_r^2}}+\mathrm{erf}\left(\frac{r}{2Dt\sqrt{\frac{1}{Dt}+\frac{4}{\lambda_r^2}}}\right)\right) \\ \times & \exp\left(\frac{r^2\lambda_r^2}{4Dt(4Dt+\lambda_r^2)}\right. \\ - & \frac{1}{4Dt(4Dt+\lambda_z^2)}\left(r^2\lambda_z^2-16D^2E_{amb}t^3\alpha_{eff}\mu\right. \\ + & \left.\left.\left.4Dt\left(r^2+z^2-2E_{amb}tz\mu+E_{amb}t(E_{amb}t\mu^2-\alpha_{eff}\lambda_z^2\mu)\right)\right)\right)\right], \end{aligned} \tag{11}$$

where $\mathrm{erf}(x) = 2/\sqrt{\pi}\int_0^x \exp(-t^2)dt$ is the Gaussian error function.

Figure 7a shows the normalized analytic density $n_e(r,z,t)/n_{e,0}$ as a function of $z$ for the different initial geometries $\lambda_r = \lambda_z = 1.5$ m, $\lambda_r = 5.25$ m, and $\lambda_z = 1.5$ m as well as $\lambda_r = 1.5$ m and $\lambda_z = 5.25$ m for $r = 0.5$ m and $E_{amb} = 1.5E_k$ at 60 km altitude. Panel (b) shows the corresponding plot for $H = 80$ km. Both panels show that the electron density from oblate patches grows larger than the electron density from spherical patches. In addition, the width of the density from the oblate patch is wider than for the density from the spherical patch. This is in agreement with our simulation results. The peak density of the electron density from the prolate patch does not grow as significantly but has a larger width due to its initial condition. As for our simulations from the oblate patch, this is in agreement with our simulation results. Note that the analytic solution (11) does not take into account the buildup of space charges, the subsequent field growth, and the feedback onto the growth of the electron density and thus differs quantitatively from our simulation results, yet there is an overall qualitative agreement.

At 60 km altitude, we have also performed simulations in a low ambient field of $0.5E_k$, but we have not observed any inception or significant development of streamer channels within approximately 100 $\mu$s; instead, only a few electron avalanches form. Figure 8 shows the on-axis electric field for two spherical patches with different size. For a fixed electron density $n_{e,0} = 5\cdot10^{11}$ m$^{-3}$ we have observed that the electric field has reached values above $1E_k$ for $\lambda_r = \lambda_z = 1.5$ m and for $\lambda_r = \lambda_z = 5.25$ m at the positive front; the field is slightly higher in the latter case. Contrarily, the peak field on the negative front is well below breakdown in both cases.

However, if we fix the initial electron number, we have observed that the field at the positive tip for the case $\lambda_r = \lambda_z = 5.25$ m is approximately $0.6E_k$, thus significantly below breakdown. This is consistent with developments of streamers in subbreakdown fields discussed by Sun et al. (2014): At the positive tip the field is focused (Liu & Pasko, 2004; Luque et al., 2008); thus, more likely to reach breakdown field strengths than on the negative front. Yet, if the initial electron-ion patch is scaled up without increasing the initial electron number simultaneously, the growth of the electric field is damped.

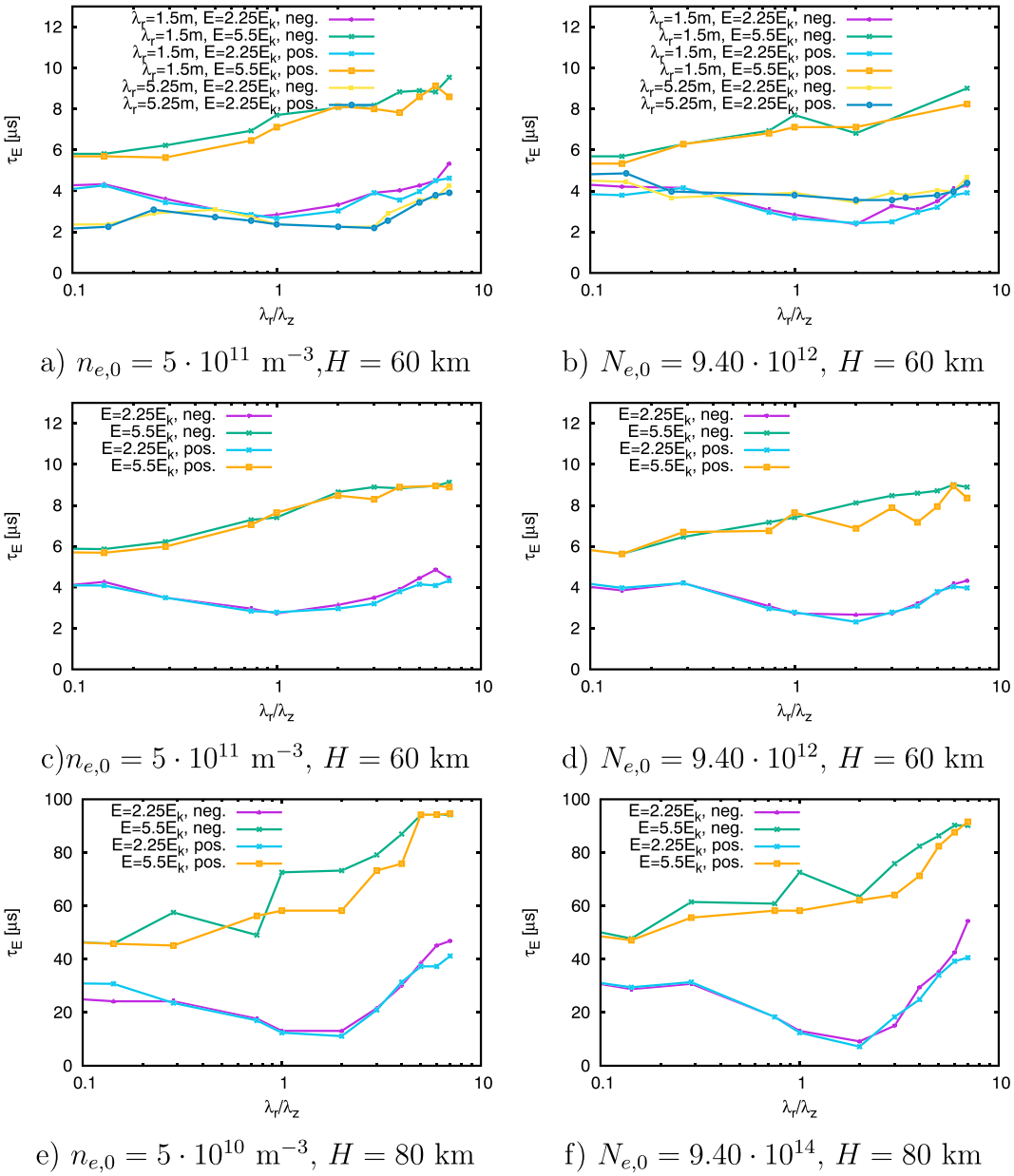


**Figure 9.** (a and b) The time $\tau_E$ for the electric field at the negative and positive front to reach $1.5E_{amb} = 2.25E_k$ and $3.7E_{amb} \approx 5.5E_k$, $E_{amb} = 1.5E_k$ at 60 km altitude, as a function of $\lambda_r/\lambda_z$, $\lambda_r = 1.5$ m for $E_{amb} = 1.5E_k$ and (a) $n_{e,0} = 5 \cdot 10^{11}$ m$^{-3}$ or (b) $N_{e,0} = 9.40 \cdot 10^{12}$. The yellow and blue lines show $\tau_E$ to reach $2.25E_k$ as a function of $\lambda_r/\lambda_z$ for $\lambda_r = 5.25$ m. (c and d) The same as in panels (a) and (b) for $\lambda_r = 1.5$ m, but for a different set of random numbers. (e and f) The time $\tau_E$ to reach $2.25E_k$ and $5.5E_k$ for $\lambda_r = 15$ m at 80 km altitude.

Thus, there are two competing conditions such that the streamer inception depends on the interplay between the size of the patch and the initial charge: The larger the initial electron-ion patch is for a fixed initial electron number, the slower the field grows whereas increasing the initial electron number facilitates the growth of the electric field at the positive front and results in a similar field evolution as for small electron-ion patches.

### 3.2. Electric Field

The development of electron avalanches and the eventual formation of streamer channels as well as branching time and ohmic heating significantly depend on the temporal evolution of the electric field. Here we discuss the electric field evolution for different patch geometries.

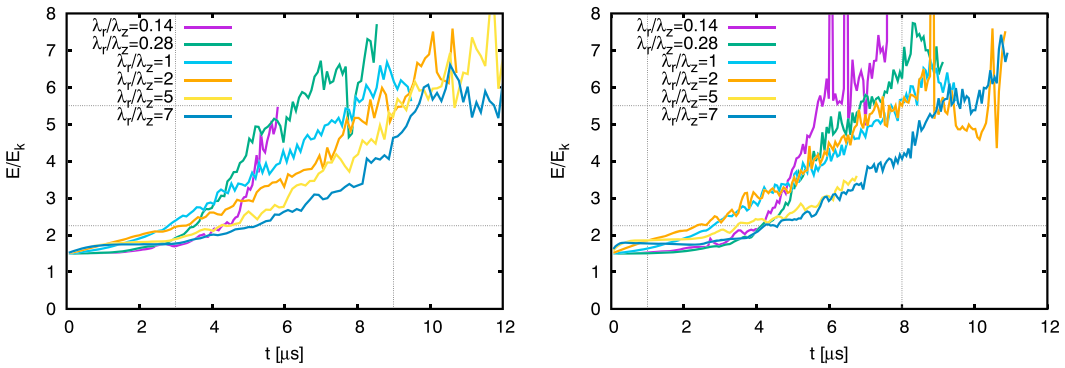


**Figure 10.** The maximum electric field strength at the negative streamer front as a function of time for (a) $n_{e,0} = 5 \cdot 10^{11}$ m$^{-3}$ and (b) $N_{e,0} = 9.40 \cdot 10^{12}$ at 60 km altitude in an ambient field of $1.5E_k$. The horizontal dotted lines indicate the field strengths $2.25E_k$ and $5.5E_k$; the vertical dotted lines indicate the time steps (a) 3 and 9 $\mu$s and (b) 1 and 8 $\mu$s.

For fixed $n_{e,0} = 5 \cdot 10^{11}$ m$^{-3}$, Figure 9a shows the time $\tau_E$ for the field to reach $1.5E_{amb} = 2.25E_k$ and $3.7E_{amb} \approx 5.5E_k$ as a function of $\lambda_r/\lambda_z$ for $\lambda_r = 1.5$ m as well as the time to reach $2.25E_k$ for $\lambda_r = 5.25$ m at 60 km altitude. While for both polarities the time $\tau_{E=5.5E_k}$ to grow up to $5.5E_k$ increases monotonically with $\lambda_r/\lambda_z$, the time $\tau_{E=2.25E_k}$ evolves nonmonotonically: First, $\tau_{E=2.25E_k}$ decreases until it reaches its minimum at approximately $\lambda_r/\lambda_z \approx 1$ for $\lambda_r = 1.5$ m and for approximately $\lambda_r/\lambda_z \approx 3$ for $\lambda_r = 5.25$ m before it increases again for increasing $\lambda_r/\lambda_z$. Figure 9b shows $\tau_E$ as in panel (a), but now for fixed $N_{e,0}$ instead of fixed density $n_{e,0}$. While the minimum of $\tau_{E=2.25E_k}$ is taken for $\lambda_r/\lambda_z \approx 1.5 - 3$ for both $\lambda_r = 1.5$ m and $\lambda_r = 5.25$ m instead of for $\lambda_r/\lambda_z \approx 1$ for fixed $n_{e,0}$, the overall trend for $\tau_E$ as a function of $\lambda_r/\lambda_z$ is the same irrespective of the initial electron number. Panels (c) and (d) show the same as in panels (a) and (b), but those simulations were performed with a different set of random numbers. We observe the same tendency as in panels (a) and (b), which excludes that the presented results are due to numerical random noise.

Panels (e) and (f) show $\tau_{E=2.25E_k}$ and $\tau_{E=5.5E_k}$ for $\lambda_r = 15$ m at 80 km altitude. We here observe the same tendency as at 60 km altitude. For $E = 2.25E_k$ the rise time is fastest for almost spherical electron-ion patches whereas the $\tau_{E=5.5E_k}$ grows linearly with $\lambda_r/\lambda_z$.

To understand why $\tau_{E=2.25E_k}$ is large for $\lambda_r/\lambda_z \lesssim 1$ or $\lambda_r/\lambda_z \gtrsim 1$ and why $\tau_{E=5.5E_k}$ increases monotonically, we regard the temporal evolution of the maximum electric field $E_{max}$. Figure 10 shows $E_{max}$ for $\lambda_r = 1.5$ m and different $\lambda_r/\lambda_z$ at 60 km altitude for fixed density (a) and fixed initial charge (b); we here identify three regimes: For $t \lesssim 3$µs (regime one) the electric field strength and its slope are largest for high ratios of $\lambda_r/\lambda_z$. This behavior changes at $t \approx 3\mu$s. For time steps $\gtrsim 3$µs and $\lesssim 8 - 9$ µs (regime two) the slope of the electric field strengths increases more strongly for small ratios of $\lambda_r/\lambda_z$ and subsequently $E_{max}$ for small $\lambda_r/\lambda_z$ exceeds $E_{max}$ for large $\lambda_r/\lambda_z$. Finally, for time steps larger than approximately $8 - 9\mu$s (regime three) the field of all considered simulations tends to $6 - 8E_k$ independent of the ratio $\lambda_r/\lambda_z$ and of the initial electron number.

The field strength $2.25E_k$ lies in the transition region between regimes 1 and 2; because of the changing slope, the electric field reaches $2.25E_k$ (lower dotted line) fastest for $\lambda_r/\lambda_z \approx 1$ and is delayed for $\lambda_r/\lambda_z \lesssim 1$ or $\lambda_r/\lambda_z \gtrsim 1$. In contrast to the early time steps, the field subsequently grows faster for small ratios of $\lambda_r/\lambda_z$. High field strengths are reached earlier for low ratios of $\lambda_r/\lambda_z$ (upper dotted line shows $5.5E_k$); hence, $\tau_{E=5.5E_k}$ increases with $\lambda_r/\lambda_z$. In all considered cases, a peak value of approx. $6 - 8E_k$ is reached irrespective of whether we keep $n_{e,0}$ or $N_{e,0}$ constant. Thus, the dependence of $\tau_E$ is affected not only by the available charge but also by the geometry of the initial electron-ion patch.

The transition from sole electron avalanches into streamer discharges strongly depends on the evolution of the electric field. Without field growth, the ionization rate does not increase, and subsequently, there is a lack of space charge driving the streamer discharge further (Ebert et al., 2006). Since $\tau_{E=5.5E_k}$ increases monotonically as a function of $\lambda_r/\lambda_z$, we expect also the avalanche-to-streamer transition to occur fastest for prolate electron-ion patches.

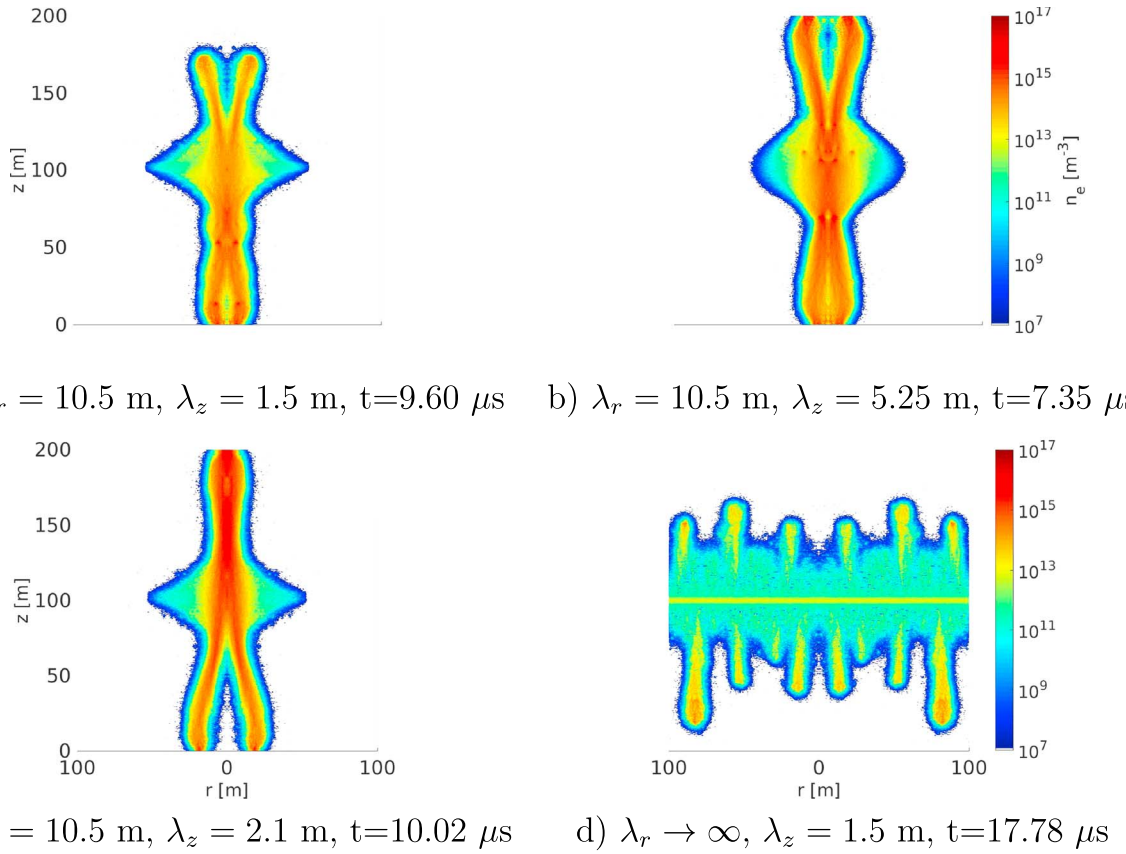


**Figure 11.** The electron density ($n_{e,0} = 5 \cdot 10^{11}$ m$^{-3}$, $E_{amb} = 1.5E_k$) at 60 km altitude for different $\lambda_r$ and $\lambda_z$ after different time steps. In all these simulations, branching occurs.

### 3.3. Branching Time

During the simulations, we have observed branching for some particular values of $\lambda_r$ and $\lambda_z$. Figure 11 shows some examples of branching at 60 km altitude for various initial conditions. We here remind the reader that we use a 2.5D Monte Carlo particle code with cylindrical symmetry. Hence, any deflection from the symmetry axis indicates branching of the streamer channel into annular structures. Although these annular structures imposed by the code after branching are not physical, the branching time is. Here we determine the branching time and the spatial distribution of the electron density briefly after branching. Figures 11a and 11b depict the electron density for $\lambda_r = 10.5$ m and $\lambda_z = 1.5$ m as well as for $\lambda_r = 10.5$ m and $\lambda_z = 5.25$ m. In these simulations, the negative front branches more easily than the positive one. On the contrary, panel (c) shows an example where the negative front does not branch, but instead, the positive one does. Panel (d) shows the electron density for streamers from a radially infinitely extended electron-ion patch, that is,$\lambda_r \to \infty$; in this case circular structures on both fronts form quickly after the inception.

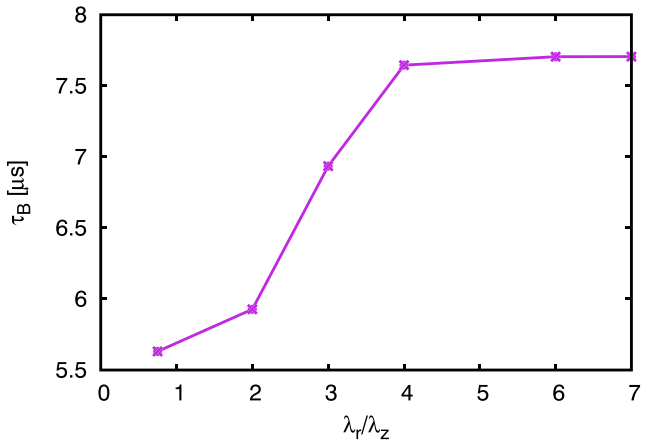


**Figure 12.** The time $\tau_B$ at 60 km altitude until the branching of the negative streamer front as a function of $\lambda_r/\lambda_z$ for $n_{e,0} = 5 \cdot 10^{11}$ m$^{-3}$ and $\lambda_r = 10.5$ m in an ambient field of $1.5E_k$.

Furthermore, panel (d) shows that, unlike for $\lambda_r \lesssim 5$ m, there is no formation of one single channel, but several structures appear simultaneously on both streamer sides for $\lambda_r \to \infty$. Note that the 2.5 code only allows us to determine if and when branching occurs; however, since the code loses its validity after branching, the density depicted in Figure 11d is not quite physical. Nonetheless, we have continued the simulation for better visibility.

Branching occurs by proximate charges repelling each other. This effect is more prominent if the total charge is enhanced over a larger region. Figure 12 shows the time $\tau_B$ until the first branching of the negative streamer front as a function of $\lambda_r/\lambda_z$ for $\lambda_r = 10.5$ m. In the multitude of simulations, we have observed branching only for $\lambda_r = 10.5$ m and only for a few $\lambda_z$. That is why we here plot only a few data points. The plot shows that branching occurs significantly later for large values of $\lambda_r/\lambda_z$, which results from the electric field evolution. As we have discussed in section 3.2, the electric field evolves more slowly for large $\lambda_r/\lambda_z$, thus decelerating the ionization of ambient air and delaying the occurrence of branching.

### 3.4. Temperature Increase and Plasma Chemistry

During the formation of streamers, electrons interact with air molecules and increase their temperature through ohmic heating. Heating involves fast processes, that is, the energy transfer from charged to neutral particles, and the delayed transfer from rotational to translational states (da Silva & Pasko, 2013). We therefore concentrate on an estimate based on the current of electrons through the channel. Since part of their energy is transferred to excitations, we here can only give an estimate of the maximum temperature increase

$$\Delta T_{max} = W/(\varrho \cdot \Delta V \cdot c_p), \tag{12}$$

where $\varrho \approx 0.4476 \cdot 10^{-3}$ kg m$^{-3}$ is the approximate mass density of air at 60 km altitude, $\Delta V$ is the volume of each grid cell, and $c_p \approx 1$ J·g$^{-1}$·K$^{-1}$ is the specific heat capacity of air. The total energy of electrons released to ambient air is given through

$$W(t) = \int_{\tilde{t}=0}^{\tilde{t}=t} \int_{V_{\text{domain}}} dV \quad d\tilde{t}\mathbf{j} \cdot \mathbf{E}, \tag{13}$$

where $\mathbf{j}$ is the current density of electrons in the field $\mathbf{E}$.

The solid line in Figure 13a shows $\Delta T_{max}$ as a function of time for $n_{e,0} = 5 \cdot 10^{11}$ m$^{-3}$, $\lambda_r = \lambda_z = 1.5$ m ($N_{e,0} = 9.40 \cdot 10^{12}$), and $E_{amb} = 1.5E_k$ at 60 km altitude. It shows that the maximum temperature increase $\Delta T_{max}$ ranges from approximately 1 $\mu$K to 0.1 K at the end of the simulation. As a comparison, the dotted line shows the temporal evolution of the temperature for the same peak density $n_{e,0}$, but for $\lambda_r = \lambda_z = 5.25$ m ($N_{e,0} = 4.03 \cdot 10^{14}$). In this simulation we see a maximum temperature increase of approximately 10 K.

Panels (b) and (c) show the ratios of different $\Delta T_{max}$ and the time derivative $d(\Delta T_{max})/dt$ for different $\lambda_r$ and $\lambda_z$ for fixed $N_{e,0}$. Panel (b) shows that in comparison to streamers from spherical electron-ion patches, the temperature increase is larger for streamers from prolate and smaller for streamers from oblate patches. This trend is confirmed by the time derivatives (c); for oblate streamers, the derivative and thus the temperature increase is smaller while it becomes larger for prolate streamers. Although we here only simulate the early stages of the streamer evolution and hence of air heating, the time derivatives in panel (c) suggest that the difference in heating for different geometries continues for larger time steps. We here point out that at the end of the simulations, we see boundary effects leading to a sudden increase of the derivatives. Nonetheless, this does not affect our interpretation of the time evolution of $\Delta T_{max}$ during the streamer motion.

The early variations in the temperature increase also affect the plasma chemistry of sprite streamers (Sentman et al., 2008). As a result of the electron motion and the electric field amplification, streamers leave behind a large population of ions as well as of dissociated and excited neutrals (Gordiollo-Vázquez, 2008), enabling chemical reactions among the constituents of air and their derivatives, that is, mainly of nitrogen and oxygen. Sentman et al. (2008) give a very detailed compilation of reactions collected from various references.

According to Arrhenius' equation, the rate coefficients $k$ of chemical reactions can be described through $k = A \cdot (T/300)^B \cdot \exp(C/T)$ with constants $A$, $B$, and $C$; hence, the efficiency of reactions significantly depends on the ambient temperature. As an example, we take the reaction $O_4^+ + O_2 \rightarrow O_2^+ + 2O_2$ (R164 in Sentman et al., 2008) at an altitude of 60 km, thus at an ambient temperature of $T_{amb} = 247.02$ K (www.engineeringtoolbox.com/standard-atmosphere-d_604.html). Then, with $T = T_{amb} + \Delta T_{max}$, it is $k(\Delta T_{max} = 10^{-1}\text{ K}) \approx 10^{-14}$ cm$^6$ s$^{-1}$ and $k(\Delta T_{max} = 10^{1}\text{ K}) \approx 2 \cdot 10^{-14}$ cm$^6$ s$^{-1}$ $\approx 2 \cdot k(\Delta T = 10^{-1}\text{ K})$; thus, the reaction is less effective for small temperatures and consequently for initial streamer geometries favoring a small electric field amplification and heating process. Similarly, the efficiency for the production of nitrogen oxides (e.g., reactions 59, 60, 70, 72, and 73 in Sentman et al., 2008) is 1.5–2 times larger for 10 K than for 0.1 K.

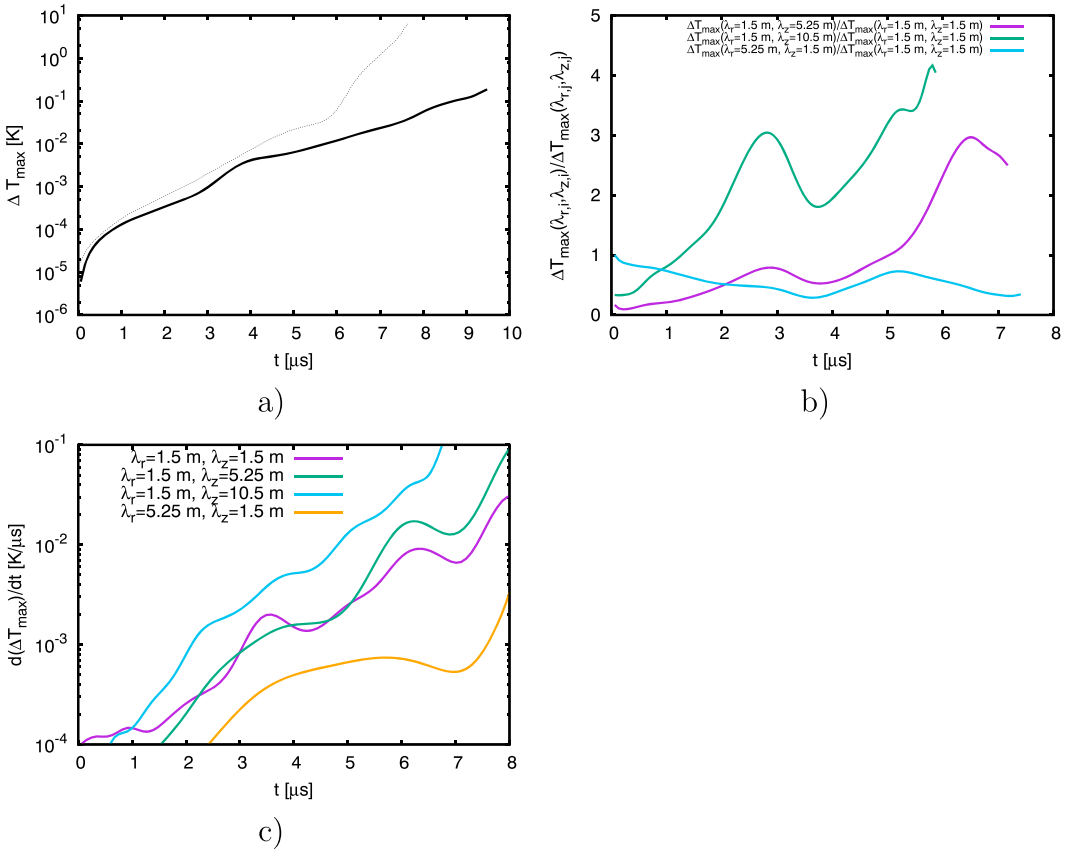


**Figure 13.** (a) The maximum temperature difference $\Delta T_{max}$ (equation (12)) associated to ohmic heating as a function of time for $n_{e,0} = 5 \cdot 10^{11}$ m$^{-3}$ and $\lambda_r = \lambda_z = 1.5$ m ($N_{e,0} = 9.40 \cdot 10^{12}$; solid line) as well as for $n_{e,0} = 5 \cdot 10^{11}$ m$^{-3}$ and $\lambda_r = \lambda_z = 5.25$ m ($N_{e,0} = 4.03 \cdot 10^{14}$; dotted line). (b and c) The ratios of different $\Delta T_{max}$ (b) and the time derivative $d(\Delta T_{max})/dt$ (c) as a function of time for different $\lambda_r$ and $\lambda_z$ for fixed $N_{e,0} = 9.40 \cdot 10^{12}$.

## 4. Discussion and Conclusions

We have investigated the inception of streamer discharges and streamer properties for spherical, oblate (pancake), and prolate (cigar) initial electron-ion patches with peak densities of $5 \cdot 10^{10} - 5 \cdot 10^{11}$ m$^{-3}$ or with an initial electron number of $9.40 \cdot 10^{12} - 9.40 \cdot 10^{14}$ in ambient fields of $0.5E_k$ and $1.5E_k$, and hence, we have estimated the effect of the shape of local electron inhomogeneities developing into sprite streamers.

For $E_{amb} = 1.5E_k$, we have calculated the temporal evolution of the electron density for different geometries. We have seen that the streamers develop faster for oblate and prolate streamers. Although this effect is more prominent when fixing the initial electron density, we have observed that the accelerated streamer fronts result from the different geometries of the initial electron-ion patch. We have also presented an analytical approximation, without space charge effects, and seen a good qualitative agreement.

Furthermore, we have calculated the temporal evolution of the electric field as a function of $\lambda_r/\lambda_z$ and seen that the time of the field to grow up to $5.5E_k$ is fastest for streamers from prolate electron-ion patches. Whereas the electric field needs approximately 6 $\mu$s at 60 km altitude and approximately 50 $\mu$s at 80 km altitude to reach $5.5E_k$ for prolate patches, this time increases for more oblate electron-ion patches. Previous calculations (Qin et al., 2013b) and high-speed videos (Cummer et al., 2006; Stenbaek-Nielsen et al., 2013) have shown that the time to generate quasi-stationary fields in the mesosphere and ionosphere, and of the early stages of streamer development, are in the order of several microseconds to tens of microseconds: Cummer et al. (2006) have observed streamer inception between 60 and 70 km altitude within tens of microseconds; Stenbaek-Nielsen et al. (2013) observed streamer inception at 66 km altitude within 150 $\mu$s. Thus, a prolate electron-ion patch, which minimizes the field growth time, facilitates the growth of the electric field and as such also the streamer inception.

For $E_{amb} = 0.5E_k$, we have not observed any avalanche-to-streamer transition within approximately 100 $\mu$s. But even for such low fields, we have observed an effect of the size and eccentricity of the initial electron-ion patch: For a constant initial electron number, smaller electron-ion patches favor the growth of the electric field at the positive front and thus facilitate the streamer inception.

Once streamers have formed, we have calculated the dependence of the branching time and ohmic heating for several initial geometries. High-speed imaging of sprite streamers (Stenbaek-Nielsen et al., 2013) has shown that branching happens within several microseconds, which is in the same order of magnitude as we have found in our simulations. For $\lambda_r = 10.5$ m, we have observed that the branching time increases with increasing $\lambda_r/\lambda_z$. Hence, the geometry of the initial electron-ion patch can partly explain the speed of branching and thus the different formation of column sprites and angle sprites resulting from different branching times. Our findings coincide with submillisecond imaging of sprites (Cummer et al., 2006), illustrating that sprites from cigar-like patches branch more quickly than sprites from a more pancake-like structure.

Not only do visible structures depend on the initial geometry but also does ohmic heating. Although additional energy losses such as excitations prevent us from determining the exact temperature increase induced by ohmic heating, we estimate that streamers of different geometries heat ambient air between some microkelvins and tens of kelvins. Whereas temperatures increase faster for streamers from prolate patches, they grow less significantly for streamers from oblate patches. Consequently, this has implications on the plasma chemistry: The initiation and the progression of chemical reactions depend on the temperature, and so does the plasma chemistry inside plasma channels. Hence, the variation of ohmic heating as a result of varying the initial patch geometries might change the production rate of chemical compounds such as nitrogen oxides.

Conclusively, our simulations have demonstrated that not only the ambient field and the available charge but also the spatial distribution of the initial charge has a significant effect on the temporal evolution of the electric field and thus on the inception and evolution of streamer channels as well as on branching and ohmic heating. We thus suggest that future streamer simulations might consider the initial geometry more carefully in order to understand these streamer related properties. This is of particular interest when comparing simulations with observations of sprites originating from nonspherical inhomogeneities, where it is thus not sufficient to start simulations from spherical electron-ion patches.

**Acknowledgments**
The research was partly funded by the Marie Curie Actions of the European Union's Seventh Framework Programme (FP7/2007-2013) under REA Grant 609405 (COFUNDPostdocDTU). This project has received funding from the European Union's Horizon 2020 Research and Innovation Programme under the Marie Sklodowska-Curie Grant 722337. The data used for this publication can be obtained from DOI:10.5281/zenodo.1327600. The authors would like to thank the reviewers whose invaluable comments have allowed significant improvement of this paper.

## References

Armstrong, R. A. (2000). Characterizing atmospheric electrodynamic emissions from lightning sprites, jets and elves. Dep. of Energy, Albuquerque Contract DE-AC04-98AL79469.

Armstrong, R. A., Suszcynsky, D. M., Lyons, W. A., & Williams, E. R. (2001). *Optical signatures, energy deposition, ionization and chemical dynamics in lightning-induced transient electrodyanamic middle and upper atmospheric events (sprites)*. Boulder, CO: Paper presented at National Radio Science Meeting, Union Radio-Sci Int.

Blanc, E., Farges, T., Brebion, D., Belyaev, A. N., Alpatov, V. V., Labarthe, A., & Melnikov, V. (2007). Main results of LSO (lightning and sprite observations) on board of the international space station. *Microgravity Science and Technology*, *19*, 80–84.

Boeck, W. L., Vaughan, O. H., Blakeslee, R. J., Vonnegut, B., & Brook, M. (1998). The role of the space shuttle videotapes in the discovery of sprites, jets and elves. *Journal of Atmospheric and Solar-Terrestrial Physics*, *60*, 669–677.

Bor, J. (2013). Optically perceptible characteristics of sprites observed in central europe in 2007-2009. *Journal of Atmospheric and Solar-Terrestrial Physics*, *92*, 151–177.

Celestin, S., & Pasko, V. P. (2011). Energy and fluxes of thermal runaway electrons produced by exponential growth of streamers during the stepping of lightning leaders and in transient luminous events. *Journal of Geophysical Research*, *116*, A03315. https://doi.org/10.1029/2010JA016260

Chanrion, O., & Neubert, T. (2008). A PIC-MCC code for simulation of streamer propagation in air. *Journal of Computational Physics*, *227*, 7222–7245.

Cummer, S. A., Jaugey, N., Li, J., Lyons, W. A., Nelson, T. E., & Gerken, E. A. (2006). Submillisecond imaging of sprite development and structure. *Geophysical Research Letters*, *33*, L04104. https://doi.org/10.1029/2005GL024969

da Silva, C. L., & Pasko, V. P. (2013). Dynamics of streamer-to-leader transition at reduced air densities and its implications for propagation of lightning leaders and gigantic jets. *Journal of Geophysical Research: Atmospheres*, *118*, 13,561–13,590. https://doi.org/10.1002/2013JD020618

da Silva, C. L., & Pasko, V. P. (2014). Infrasonic acoustic waves generated by fast air heating in sprite cores. *Geophysical Research Letters*, *41*, 1789–1795. https://doi.org/10.1002/2013GL059164

Ebert, U., Montijn, C., Briels, T. M. P., Hundsdorfer, W., Meulenbroek, B., Rocco, A., & van Veldhuizen, E. M. (2006). The multiscale nature of streamers. *Plasma Sources Science and Technology*, *15*, S118.

Ebert, U., & Sentman, D. D. (2008). Streamers, sprites, leaders, lightning: From micro- to macroscales. *Journal of Physics D: Applied Physics*, *41*, 23.

Franz, R. C., Nemzek, R. J., & Winckler, J. R. (1990). Television image of large upward electrical discharge above a thunderstorm system. *Science*, *249*, 48–51.
Gordiollo-Vázquez, F. J. (2008). Air plasma kinetic under the influence of sprites. *Journal of Physics D: Applied Physics*, *41*, 234016.
Köhn, C., Chanrion, O., & Neubert, T. (2017). The influence of bremsstrahlung on electric discharge streamers in $N_2$, $O_2$ gas mixtures. *Plasma Sources Science and Technology*, *26*, 15006.
Kosar, B. C., Liu, N., & Rassoul, H. K. (2012). Luminosity and propagation characteristics of sprite streamers initiated from small ionospheric disturbances at subbreakdown conditions. *Journal of Geophysical Research*, *117*, A08328. https://doi.org/10.1029/2012JA017632
Kosar, B. C., Liu, N., & Rassoul, H. K. (2013). Formation of sprite streamers at subbreakdown conditions from ionospheric inhomogeneities resembling observed sprite halo. *Geophysical Research Letters*, *40*, 6282–6287. https://doi.org/10.1002/2013GL058294
Kossyi, I. A., Kostinsky, A. Y., Matveyev, A. A., & Silakov, V. P. (1992). Kinetic scheme of the non-equilibrium discharge in nitrogen-oxygen mixtures. *Plasma Sources Science and Technology*, *1*, 207220.
Li, C., Ebert, U., & Brok, W. J. M. (2008). Avalanche-to-streamer transition in particle simulations. *IEEE Transactions on Plasma Science*, *36*, 910–911.
Liu, N., Dwyer, J. R., Stenbaek-Nielsen, H. C., & McHarg, M. G. (2015). Sprite streamer initiation from natural mesospheric structures. *Nature Communications*, *6*, 7540.
Liu, N., Kosar, B. C., Sadighi, S., Dwyer, J. R., & Rassoul, H. K. (2012). Formation of streamer discharges from an isolated ionization column at subbreakdown conditions. *Physical Review Letters*, *109*, 25002.
Liu, N., & Pasko, V. P. (2004). Effects of photoionization on propagation and branching of positive and negative streamers in sprites. *Journal of Geophysical Research*, *109*, A04301. https://doi.org/10.1029/2003JA010064
Luque, A., & Ebert, U. (2009). Emergence of sprite streamers from screening-ionization waves in the lower ionosphere. *Nature Geoscience*, *2*, 757–760.
Luque, A., & Ebert, U. (2010). Sprites in varying air density: Charge conservation, glowing negative trails and changing velocity. *Geophysical Research Letters*, *37*, L06806. https://doi.org/10.1029/2009GL041982
Luque, A., Ratushnaya, V., & Ebert, U. (2008). Positive and negative streamers in ambient air: Modelling evolution and velocities. *Journal of Physics D: Applied Physics*, *41*, 234005.
Lyons, W. A. (1996). Sprite observations above the U.S. high plains in relation to their parent thunderstorm system. *Journal of Geophysical Research*, *11*, 641–652.
McHarg, M. G., Haaland, R. K., Moudry, D., & Stenbaek-Nielsen, H. C. (2002). Altitude-time development of sprites. *Journal of Geophysical Research*, *107*, 1364. https://doi.org/10.1029/2001JA000283
Meek, J. M. A. (1940). A theory of spark discharge. *Physical Review*, *57*, 722–728.
Neubert, T. (2003). On sprites and their exotic kin. *Science*, *300*, 741–749.
Pasko, V. P. (2007). Red sprite discharges in the atmosphere at high altitude: The molecular physics and the similarity with laboratory discharges. *Plasma Sources Science and Technology*, *16*, S13.
Pasko, V. P. (2008). Blue jets and gigantic jets: Transient luminous events between thunderstorm tops and the lower ionosphere. *Plasma Physics and Controlled Fusion*, *50*, 124050.
Pasko, V. P., Inan, U. S., & Bell, T. F. (2000). Fractal structure of sprites. *Geophysical Research Letters*, *27*, 497–500.
Pasko, V. P., Inan, U. S., Bell, T. F., & Taranenko, Y. N. (1997). Sprites produced by quasi-electrostatic heating and ionization in the lower ionosphere. *Journal of Geophysical Research*, *102*, 4529–4561.
Pasko, V. P., Inan, U. S., Taranenko, Y. N., & Bell, T. F. (1995). Heating, ionization and upward discharges in the mesosphere due to intense quasi-electrostatic thundercloud fields. *Geophysical Research Letters*, *22*, 365–368.
Pasko, V. P., Qin, J., & Celestin, S. (2013). Toward better understanding of sprite streamers: Initiation, morphology, and polarity asymmetry. *Surveys in Geophysics*, *34*, 797–830.
Qin, J., Celestin, S., & Pasko, V. P. (2012). Formation of single and double-headed streamers in sprite-halo events. *Geophysical Research Letters*, *39*, L05810. https://doi.org/10.1029/2012GL051088
Qin, J., Celestin, S., & Pasko, V. P. (2013a). Dependence of positive and negative sprite morphology on lightning characteristics and upper atmospheric ambient conditions. *Journal of Geophysical Research: Space Physics*, *118*, 2623–2638. https://doi.org/10.1029/2012JA017908
Qin, J., Celestin, S., Pasko, V. P., Cummer, S. A., McHarg, M. G., & Stenbaek-Nielsen, H. C. (2013b). Mechanism of column and carrot sprites derived from optical and radio observations. *Geophysical Research Letters*, *40*, 4777–4782. https://doi.org/10.1002/grl.50910
Qin, J., Pasko, V. P., McHarg, M. G., & Stenbaek-Nielsen, H. C. (2014). Plasma irregularities in the d-region ionosphere in association with sprite streamer initiation. *Nature Communications*, *5*, 3740.
Raether, H. (1939). Die Entwicklung der Elektronen in den Funkenkanal. *Zeitschrift für Physik*, *112*, 464–489.
Raizer, Y. P. (1991). *Gas Discharge Physics*. Berlin, Heidelberg: Springer-Verlag.
Rodger, C. J., Seppälä, A., & Clilverd, M. A. (2008). Significance of transient luminous events to neutral chemistry: Experimental meausrements. *Geophysical Research Letters*, *35*, L07803. https://doi.org/10.1029/2008GL033221
Sentman, D. D., Stenbaek-Nielsen, H. C., McHarg, M. G., & Morrill, J. S. (2008). Plasma chemistry of sprite streamers. *Journal of Geophysical Research*, *113*, D11112. https://doi.org/10.1029/2007JD008941
Sentman, D. D., Wescott, E. M., Osborne, D. L., Hampton, D. L., & Heavner, M. J. (1995). Preliminary results from the sprites94 campaign: Red sprites. *Geophysical Research Letters*, *22*, 1205–1208.
Stenbaek-Nielsen, H. C., Kanmae, T., McHarg, M. G., & Haaland, R. (2013). High-speed observations of sprite streamers. *Surveys in Geophysics*, *34*, 769–795.
Stenbaek-Nielsen, H. C., Moudry, D. R., Wescott, E. M., Sentman, D. D., & São S. (2000). Sprites and possible mesospheric effects. *Geophysical Research Letters*, *27*, 3829–3832.
Su, H. T., Hsu, R. R., Chen, A. B., Mende, S. B., Rairden, R. L., Allin, T. H., & Neubert, T. (2002). Observation of angle sprites. *COSPAR Colloquia Series*, *12*, 289–294.
Sun, A., Teunissen, J., & Ebert, U. (2014). The inception of pulsed discharges in air: Simulations in background fields above and below breakdown. *Journal of Physics D: Applied Physics*, *47*, 445205.
Suszcynsky, D. M. R., Strabley, R., Roussel-Dupre, R., Symbalisty, E. M. D., Armstrong, R. A., Lyons, W. A., & Taylor, M. (1999). Video and photometric observations of a sprite in coincidence with a meteor-triggered jet event. *Journal of Geophysical Research*, *104*, 31,361–31,367.
Vaughan, O. H., & Vonnegut, B. (1989). Recent observations of lightning discharges from the top of a thundercloud into the clear air above. *Journal of Geophysical Research*, *94*, 13,179–13,182.
Wilson, C. T. R. (1925). The electric field of a thundercloud and some of its effects. *Proceedings of the Physical Society of London*, *37*, 32D–37D.

Winkler, H., & Notholt, J. (2014). The chemistry of daytime sprite streamers—A model study. *Atmospheric Chemistry and Physics*, *14*, 3545–3556.

Yair, Y., Price, C., Levin, Z., Joseph, J., Isrealevitch, P., & Devir, A. (2003). Sprite observations from the space shuttle during the mediterranean Israeli dust experiment (MEIDEX). *Journal of Atmospheric and Solar-Terrestrial Physics*, *65*, 635–642.